Title

Characterization of serial hyperpolarized 13C metabolic imaging in patients with glioma

Authors

Autry, Adam W

Gordon, Jeremy W

Chen, Hsin-Yu

et al.

Publication Date

2020

DOI

10.1016/j.nicl.2020.102323

Peer reviewed

NeuroImage: Clinical 27 (2020) 102323

Contents lists available at ScienceDirect

NeuroImage: Clinical

journal homepage: www.elsevier.com/locate/ynicl

Characterization of serial hyperpolarized ^{13}C metabolic imaging in patients with glioma

Adam W. Autry[a], Jeremy W. Gordon[a], Hsin-Yu Chen[a], Marisa LaFontaine[a], Robert Bok[a], Mark Van Criekinge[a], James B. Slater[a], Lucas Carvajal[a], Javier E. Villanueva-Meyer[a], Susan M. Chang[b], Jennifer L. Clarke[b], Janine M. Lupo[a], Duan Xu[a], Peder E.Z. Larson[a], Daniel B. Vigneron[a,c], Yan Li[a,*]

[a] Department of Radiology and Biomedical Imaging, University of California San Francisco, San Francisco, USA
[b] Department of Neurological Surgery, University of California San Francisco, San Francisco, USA
[c] Department of Bioengineering and Therapeutic Sciences, University of California San Francisco, San Francisco, USA

ARTICLE INFO

Keywords:
Hyperpolarized
Carbon-13
Metabolism
Kinetics
Glioma
Bevacizumab

ABSTRACT

Background: Hyperpolarized carbon-13 (HP-^{13}C) MRI is a non-invasive imaging technique for probing brain metabolism, which may improve clinical cancer surveillance. This work aimed to characterize the consistency of serial HP-^{13}C imaging in patients undergoing treatment for brain tumors and determine whether there is evidence of aberrant metabolism in the tumor lesion compared to normal-appearing tissue.

Methods: Serial dynamic HP [1-^{13}C]pyruvate MRI was performed on 3 healthy volunteers (6 total examinations) and 5 patients (21 total examinations) with diffuse infiltrating glioma during their course of treatment, using a frequency-selective echo-planar imaging (EPI) sequence. HP-^{13}C imaging at routine clinical timepoints overlapped treatment, including radiotherapy (RT), temozolomide (TMZ) chemotherapy, and anti-angiogenic/investigational agents. Apparent rate constants for [1-^{13}C]pyruvate conversion to [1-^{13}C]lactate (k_{PL}) and [^{13}C]bicarbonate (k_{PB}) were simultaneously quantified based on an inputless kinetic model within normal-appearing white matter (NAWM) and anatomic lesions defined from ^{1}H MRI. The inter/intra-subject consistency of $k_{PL\text{-}NAWM}$ and $k_{PB\text{-}NAWM}$ was measured in terms of the coefficient of variation (CV).

Results: When excluding scans following anti-angiogenic therapy, patient values of $k_{PL\text{-}NAWM}$ and $k_{PB\text{-}NAWM}$ were 0.020 s^{-1} ± 23.8% and 0.0058 s^{-1} ± 27.7% (mean ± CV) across 17 HP-^{13}C MRIs, with intra-patient serial $k_{PL\text{-}NAWM}/k_{PB\text{-}NAWM}$ CVs ranging 6.8–16.6%/10.6–40.7%. In 4/5 patients, these values (0.018 s^{-1} ± 13.4% and 0.0058 s^{-1} ± 24.4%; n = 13) were more similar to those from healthy volunteers (0.018 s^{-1} ± 5.0% and 0.0043 s^{-1} ± 12.6%; n = 6) (mean ± CV). The anti-angiogenic agent bevacizumab was associated with global elevations in apparent rate constants, with maximum $k_{PL\text{-}NAWM}$ in 2 patients reaching 0.047 ± 0.001 and 0.047 ± 0.003 s^{-1} (± model error). In 3 patients with progressive disease, anatomic lesions showed elevated k_{PL} relative to $k_{PL\text{-}NAWM}$ of 0.024 ± 0.001 s^{-1} (± model error) in the absence of gadolinium enhancement, and 0.032 ± 0.008, 0.040 ± 0.003 and 0.041 ± 0.009 s^{-1} with gadolinium enhancement. The lesion k_{PB} in patients was reduced to unquantifiable values compared to $k_{PB\text{-}NAWM}$.

Conclusion: Serial measures of HP [1-^{13}C]pyruvate metabolism displayed consistency in the NAWM of healthy volunteers and patients. Both k_{PL} and k_{PB} were globally elevated following bevacizumab treatment, while progressive disease demonstrated elevated k_{PL} in gadolinium-enhancing and non-enhancing lesions. Larger prospective studies with homogeneous patient populations are planned to evaluate metabolic changes following treatment.

Abbreviations: HP-^{13}C, hyperpolarized carbon-13; DNP, dynamic nuclear polarization; RT, radiotherapy; TMZ, temozolomide; PDH, pyruvate dehydrogenase; LDH, lactate dehydrogenase; CA, carbonic anhydrase

* Corresponding author at: Department of Radiology and Biomedical Imaging, University of California San Francisco, 185 Berry Street, Ste. 350, San Francisco, CA 94107, USA.
E-mail address: yan.li@ucsf.edu (Y. Li).

https://doi.org/10.1016/j.nicl.2020.102323
Received 28 April 2020; Received in revised form 15 June 2020; Accepted 21 June 2020
Available online 24 June 2020

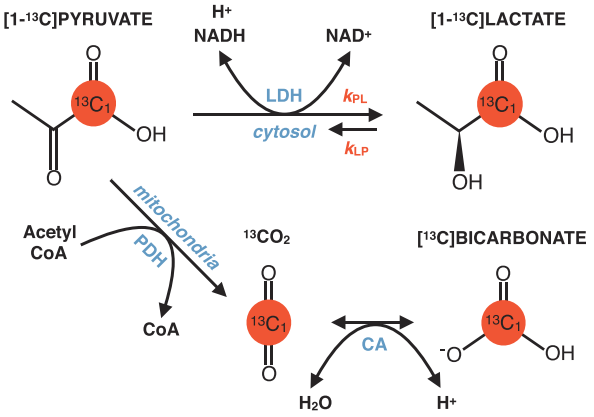

Fig. 1. HP [1-^{13}C] pyruvate brain metabolism. Diagram of HP [1-^{13}C]pyruvate metabolism in the brain, which is characterized by two primary pathways: enzymatic conversion of [1-^{13}C]pyruvate to [1-^{13}C]lactate via cytosolic lactate dehydrogenase (LDH); and successive conversion of [1-^{13}C]pyruvate to $^{13}CO_2$ and [^{13}C]bicarbonate via mitochondrial pyruvate dehydrogenase (PDH) and carbonic anhydrase (CA), respectively. The second-order kinetics of pyruvate-to-bicarbonate conversion are approximated by the rate-limiting step of PDH, given the rapid CO_2-bicarbonate exchange catalyzed by CA. HP [1-^{13}C] pyruvate is also reversibly converted to [1-^{13}C]alanine via alanine transaminase (ALT), but prior studies have shown that conversion to HP [1-^{13}C]alanine occurs outside of the brain (4).

1. Introduction

Dynamic hyperpolarized carbon-13 (HP-^{13}C) MRI has emerged as a powerful technique for non-invasively probing *in vivo* metabolism in real time. By utilizing specialized instrumentation to transiently enhance the signal of ^{13}C nuclei via dynamic nuclear polarization (DNP), HP-^{13}C imaging provides the ability to detect metabolic conversion of labeled molecules following their intravenous injection (Ardenkjaer-Larsen et al., 2003).

Among the diverse applications of HP-^{13}C imaging, interrogating brain metabolism remains a principal investigational interest. After demonstrating the feasibility of using HP [1-^{13}C]pyruvate as a molecular probe in preclinical animal studies (Golman et al., 2006; Park et al., 2014); early human trials importantly showed that this molecule is safely and rapidly transported across the blood brain barrier (BBB) over experimental timescales (Park et al., 2018; Miloushev et al., 2018). In the human brain, HP [1-^{13}C]pyruvate undergoes enzymatic conversion to [1-^{13}C]lactate via cytosolic lactate dehydrogenase (LDH) and [^{13}C]bicarbonate via mitochondrial pyruvate dehydrogenase (PDH) and carbonic anhydrase (CA), thus providing an unprecedented means of probing glycolytic and oxidative phosphorylation pathways (Fig. 1) (Lunt and Vander Heiden, 2011; Saraste, 1999). Recent studies in healthy volunteers have reported on the regional variation of brain metabolism, as well as patterns of metabolite production that are conserved over a wide age range (Grist et al., 2019; Lee et al., 2020).

Given the potential for highlighting aberrant cancer metabolism, particular emphasis has been placed on characterizing HP-^{13}C imaging in patients with gliomas (Park et al., 2018; Miloushev et al., 2018). Diffuse infiltrating gliomas comprise a heterogeneous class of brain tumors, which are graded according to malignancy using histopathologic and molecular criteria (Louis et al., 2016). While the most common and aggressive form of this disease is grade IV glioblastoma (GBM), patients who are initially diagnosed with grade II or III glioma may undergo malignant transformation to higher grades (Chaichana et al., 2010). In the case of GBM, standard-of-care treatment currently includes maximal surgical resection, radiation therapy (RT) and concurrent temozolomide (TMZ) chemotherapy, followed by 6 months of adjuvant TMZ (Stupp et al., 2005). Since the effects of standard and adjuvant therapies can often mimic or even mask disease using routine anatomic ^{1}H MRI, HP-^{13}C imaging may assist in monitoring response to treatment (Winter et al., 2019; Da Cruz et al., 2011).

The purpose of the current study was to characterize serial dynamic HP-^{13}C imaging using a kinetic modeling approach (Larson et al., 2018) in healthy volunteers and patients who received treatment for glioma. Apparent [1-^{13}C]pyruvate metabolism within NAWM was compared in volunteers versus patients and evaluated for variation across examinations, while metabolism within tumor lesions was assessed for alterations relative to NAWM.

2. Methods

2.1. ^{13}C hardware and calibration

All experiments were performed on a clinical 3 T whole body scanner (MR 750; GE Healthcare, Waukesha, WI) equipped with 32-channel multi-nuclear imaging capability. Details of the ^{13}C receiver and transmit coil hardware are contained in Supplementary Fig. 1. Transmit RF power (TG) was calibrated using a ^{13}C FID sequence with a non-slice selective 90° pulse (GE Healthcare) on a head-shaped phantom containing unenriched ethylene glycol ($HOCH_2CH_2OH$, anhydrous, 99.8%, Sigma Aldrich, St. Louis, MO), doped with 17 g/L (0.29 M) NaCl to recapitulate physiological loading (Autry et al., 2019).

2.2. Subject population and treatment

Three healthy volunteers and five patients previously diagnosed with infiltrating glioma (WHO grades II-IV) were recruited to the IRB-approved study following informed consent at the University of California, San Francisco (Table 1). While the treatments prior to HP-^{13}C imaging varied across the patients, all had undergone surgery (5/5) and a few had received chemoradiotherapy (RT/TMZ) (2/5) as shown in Table 1. Over the course of serial HP-^{13}C imaging, some patients had additional surgery (2/5), RT/TMZ (1/5), adjuvant RT (3/5), bevacizumab (2/5), and other therapies further detailed in Table 1. Supplementary Fig. 2 depicts individual patient treatment timelines and their intervals of HP-^{13}C imaging.

2.3. Sample polarization and QC

Hyperpolarization of [1-^{13}C]pyruvate was performed on a SPINlab system (General Electric, Niskayuna, NY) designed for clinical applications (Park et al., 2018). In order to maintain an ISO 5 environment, pharmacists utilized an isolator (Getinge Group, Getinge, France) and clean bench laminar flow hood for preparing pharmacy kits. Pharmacy kits filled with a mixture of 1.432 g [1-^{13}C]pyruvic acid (MilliporeSigma, Miamisburg, OH) and 28 mg electron paramagnetic agent (EPA) (AH111501; GE Healthcare, Oslo, Norway) were loaded into the SPINlab and polarized for at least 2.5 h with 140 GHz microwave radiation at 5 T and 0.8 K. Following polarization, the pyruvate and trityl radical solution was rapidly dissolved in sterile water and passed through a filter under pressure to achieve a residual trityl concentration of < 3 μM. This solution was then collected in a receiver vessel, neutralized, and diluted with a sodium hydroxide tris(hydroxymethyl) aminomethane/ethylenediaminetetraacetic acid buffer solution. An integrated quality control (QC) system rapidly measured the resulting pH, temperature, residual EPA concentration, volume, pyruvate concentration, and polarization level. Upon completing the QC analysis, the sample underwent terminal sterilization in a filter (0.2 μm; ZenPure, Manassas, VA) before being collected in a MEDRAD syringe (Bayer HealthCare, Pittsburgh, PA).

Acceptable compounding tolerances for pharmacist release of the sample were: 1) polarization $\geq$15%; 2) pyruvate concentration, 220–280 mM; 3) EPA concentration $\leq$3.0 μM; 4) pH, 5.0–9.0; 5) temperature, 25–37 °C; 6) volume > 38 mL; and 7) bubble point test on sterilizing filter passed at 50 psi. The injected volume of HP [1-^{13}C]

Table 1
Subject population. Subject demographics, clinical characterization, and lesion volume for healthy volunteers (HV) and patients (P). IDH, isocitrate dehydrogenase; GBM, glioblastoma; NA, not applicable; Sx, surgery; CCNU, lomustine; RT, radiation therapy; TMZ, temozolomide.

Subject ID	Diagnosis	Prior disease status	Age (yr), Sex	No. serial scans (total timespan)	Prior treatment	Treatment at the time of imaging	T2L, CEL volume (cm^3)
HV1	NA	NA	41 M	1	NA	NA	NA
HV2	NA	NA	59 M	2 (30 min)	NA	NA	NA
HV3	NA	NA	40F	3 (174 dy)	NA	NA	NA
P1	IDH mutant anaplastic oligodendroglioma	Recurrent	52 M	3 (578 dy)	2 Sx, RT/TMZ, TMZ, CCNU	Sx, RT	8–16, < 1
P2	IDH mutant GBM	Recurrent	30F	9 (512 dy)	3 Sx	RT/TMZ, bevacizumab, pembrolizumab, CCNU, carboplatin	17–124, < 1–6
P3	IDH mutant GBM	Recurrent	42 M	3 (301 dy)	2 Sx, RT/TMZ, TMZ, bevacizumab	Bevacizumab	27–47, 6–12
P4	IDH mutant oligodendroglioma	Non-Recurrent	49F	2 (224 dy)	Sx	None	44–87, 0
P5	IDH wildtype GBM	Recurrent	55F	4 (225 dy)	Sx, RT/TMZ, veliparib/placebo	Sx, RT pembrolizumab	26–175, 2–12

pyruvate was based on a 0.43 mL/kg dosage, delivered at a rate of 5 mL/s, and followed by a 20 mL sterile saline flush at the same rate. Supplementary Table 1 contains the experimental QC and injection parameters, summarized as follows by the mean and range of values: polarization, 41% (36–51%); pyruvate concentration, 238 mM (216–255 mM); EPA concentration, 1.1 μM (0.3–2.4 μM); pH, 7.5 (6.1–8.3); temperature, 32 °C (29–36 °C); volume, 29 mL (20–40 mL); time-to-injection, 58 s (49–83 s).

2.4. Serial imaging protocol

After confirming that patient vital signs permitted administration of HP contrast, an intravenous catheter was placed in the antecubital vein. T_2-weighted fast spin echo (FSE) images (TR/TE = 4000/60 ms, FOV = 26 cm, 192 × 256 matrix, 5 mm slice thickness, and NEX = 2) acquired with the ^{1}H body coil or dual-tuned ^{13}C/^{1}H hardware configuration served as an anatomic reference for prescribing ^{13}C sequences. An embedded 1 mL 8 M ^{13}C-urea sample in the receiver array provided *in vivo* frequency referencing for [1-^{13}C]pyruvate: $f_{pyruvate} = f_{urea} + 270$ Hz. Following pharmacist approval of sample safety, patients were injected with the HP [1-^{13}C]pyruvate and dynamic HP-^{13}C echo-planar imaging (EPI) data were acquired beginning 5 s after the end of the saline flush to allow for cerebral bolus arrival.

A frequency-selective 2D multislice EPI sequence (TR/TE = 62.5 ms/21.7 ms, 24 × 24 cm^2 FOV, 1032 μs echo-spacing, ± 10 kHz BW, 8 slices, 20 timepoints, 3 s temporal resolution, 60 s total acquisition time) with 2–8 cm^3 spatial resolution (3.38 cm^3 for 76% of scans) was acquired for each subject (Gordon et al., 2017; Gordon et al., 2019). Individual [1-^{13}C]pyruvate, [1-^{13}C]lactate, and [^{13}C]bicarbonate resonances were sequentially excited using a single-band spectral-spatial (SPSP) RF pulse (130 Hz FWHM, 868 Hz stopband peak-to-peak) over interleaved acquisitions with a variable flip angle scheme that was constant through time (67% of scans utilized [α_{pyr}, α_{lac}, α_{bic}] = [20°, 30°, 30°]). The [1-^{13}C]alanine resonance was not acquired as prior studies have shown that it is only present in subcutaneous tissue and muscle outside the brain (Park et al., 2018). Supplementary Table 2 contains the complete set of acquisition parameters for each EPI scan. Noise-only data were acquired separately prior to each HP injection. To measure relative metabolite frequencies for quality assurance, non-localized spectra (TR = 3 s, θ = 60°, 8 time points) were immediately acquired after the first scan with a 500 μs hard pulse.

After this scan, post-injection vital signs were measured and patients received a routine ^{1}H MR examination using the same dual-tuned hardware configuration (8-channel) or a 32-channel ^{1}H coil (Nova Medical Inc., Wilmington, MA). This exam included pre- and post-gadolinium contrast 3D T_1-weighted IRSPGR images (TR/TE/TI = 6636/2468/450 ms, resolution = 1.5 × 1 × 1 mm^3, 25.6 cm FOV, 256 × 256 matrix) and 3D T_2-weighted FLAIR images (TR/TE/TI = 6250/138/1702 ms, resolution = 1.5 × 1 × 1 mm^3, 25.6 cm FOV, 256 × 256 matrix).

2.5. ROI segmentation

For each ^{1}H exam, white matter was segmented on the pre-contrast T_1-weighted images using the FSL FAST algorithm (Zhang et al., 2001), and the FLAIR T_2-hyperintense lesion (T2L) and post-gadolinium contrast-enhancing lesion (CEL) were manually segmented by a trained researcher with 3D Slicer software (Menze et al., 2015). A normal-appearing white matter (NAWM) mask was generated by subtracting the T2L from the segmented white matter. In cases where data was not acquired with dual-tuned ^{1}H/^{13}C hardware, ^{1}H images and ROIs were aligned to the body coil T_2-weighted FSE images acquired during the ^{13}C exam using FSL FLIRT (Jenkinson and Smith, 2001). Individual ^{13}C data voxels were exclusively categorized as NAWM or T2L/CEL when at least 30% of their volume contained the ^{1}H ROIs. This was

accomplished by subtracting the designated ^{13}C voxels of the lesion (T2L/CEL) from those of the NAWM.

2.6. Post-processing of ^{13}C data

Raw dynamic EPI data were routinely processed by first determining the phase coefficients for removing ghosting artifacts (Wang et al., 2017). Noise decorrelation via Cholesky decomposition was employed to improve channel decoupling and the signal-to-noise ratio (SNR) prior to EPI reconstruction (Pruessmann et al., 2001). Coil combination was performed using complex weights derived from the pyruvate data (Zihan et al., 2019). The data were finally phased for each metabolite to provide zero-mean Gaussian noise for model-based fitting (Crane et al., 2020). Software used in this study are available online via the "Hyperpolarized MRI Toolbox" on Github (Crane et al., 2020).

2.7. Kinetic modeling

Apparent rate constants for pyruvate-to-lactate (k_{PL}) and pyruvate-to-bicarbonate (k_{PB}) conversion were quantified using an "inputless" model (Larson et al., 2018), which approximated first-order kinetics. While accounting for differences in applied flip angles, this model simultaneously fit phased dynamic data from [1-^{13}C]lactate and [^{13}C] bicarbonate signals that had been summed over NAWM and T2L/CEL ROIs. Error in reported k_{PL} and k_{PB} values was estimated from nonlinear least squares residuals of the associated fitting and thresholded above 25%. Dynamic EPI data were also fit in a voxel-wise fashion to generate apparent rate constant maps for visualization, when the total SNR was > 3 for each metabolite. Illustrative k_{PL} and k_{PB} maps from a patient with GBM are shown together with corresponding dynamic traces and ROIs in Fig. 2.

2.8. Analysis

To evaluate the consistency of $k_{PL\text{-}NAWM}$ and $k_{PB\text{-}NAWM}$ values across serial scans and subjects, the coefficients of variation (CVs; SD/mean) were calculated and expressed as percentages. Rate constant values were qualitatively compared between NAWM and T2L/CEL.

3. Results

3.1. Healthy volunteers

Fig. 3A presents example dynamic EPI k_{PL} and k_{PB} maps from a healthy volunteer, which demonstrate the spatial variation of apparent HP [1-^{13}C]pyruvate metabolism. By comparison to the cortex, cuneus and deep gray structures, white matter displayed relatively lower apparent conversion rates, as modeled by both k_{PL} and k_{PB} (Fig. 3A). While coverage of the k_{PB} map was limited by the SNR of [^{13}C]bicarbonate deep within the brain, k_{PL} and k_{PB} values were seen to spatially trend together (Fig. 3A). The 3 healthy volunteers (1 female, 2 male) who ranged 40–59 years-of-age (Table 1) collectively showed similar kinetic profiles within NAWM over a total of 6 scans: $k_{PL\text{-}NAWM}$ = 0.018 s^{-1} ± 5.0% (0.016–0.018 s^{-1}) and $k_{PB\text{-}NAWM}$ = 0.0043 s^{-1} ± 12.6% (0.0035–0.0049 s^{-1}) [mean ± CV (range)] (Fig. 3B; Table 2). Despite differences in receiver hardware over scan intervals ranging from 30 min to 107 days, healthy volunteers HV2 and HV3 further demonstrated consistency in serial k_{PL} and k_{PB} values (Fig. 3B; Table 2).

3.2. Serial patients

A total of 21 serial HP-^{13}C imaging exams were performed on the 5 patients (3 female, 2 male) who ranged 30–55 years-of-age. Table 1 presents a summary of diagnosis, clinical features, and treatment history for each patient. Infiltrating gliomas in this cohort spanned the range of disease aggressiveness and represented diverse histopathology: 1 IDH-mutant grade II oligodendroglioma; 1 IDH-mutant anaplastic oligodendroglioma; and 3 grade IV GBM (2 IDH-mutant/1 IDH-wild-type) (Table 1) (Yan et al., 2019). Over the course of imaging, 3 patients received RT and/or TMZ and 2 patients received the anti-angiogenic agent bevacizumab as part of their treatment.

Table 2 provides a summary overview of the serial HP-^{13}C kinetic data for each patient, as quantified within the NAWM, T2L, and CEL, together with the associated serial CVs. When excluding scans that overlapped anti-angiogenic therapy, the mean $k_{PL\text{-}NAWM}$ and $k_{PB\text{-}NAWM}$ over the remaining 17 of 21 scans were 0.020 s^{-1} ± 23.8% (0.015–0.029 s^{-1}) and 0.0058 s^{-1} ± 27.7% (0.0037–0.0078 s^{-1}) [mean ± CV(range)], and intra-patient serial $k_{PL\text{-}NAWM}/k_{PB\text{-}NAWM}$ demonstrated consistency with CVs ranging 6.8–16.6%/10.6–40.7% (Table 2). In particular, for patients P1-4, values of $k_{PL\text{-}NAWM}$ = 0.018 s^{-1} ± 13.4% (0.015–0.022 s^{-1}) and $k_{PB\text{-}NAWM}$ = 0.0058 s^{-1} ± 24.4% (0.0037–0.0078 s^{-1}) [n = 13; mean ± CV(range)] were more similar to those of healthy volunteers, while patient P5 displayed consistently higher $k_{PL\text{-}NAWM}$ = 0.028 s^{-1} ± 7.1% (mean ± CV) over 4 scans spanning 225 days (Table 2). When the acquired spatial resolution was 1.5 cm isotropic or lower and the flip angle scheme was maintained over serial imaging, $k_{PL\text{-}NAWM}$ and $k_{PB\text{-}NAWM}$ CVs were as low as 6.8% and 10.8%, respectively, for 6 scans (patient P2).

In the two patients with limited to no treatment during imaging (P4 and P1), the mean apparent rate constants in NAWM were comparable to that of healthy volunteers. Patient P4, who only received surgical treatment prior to serial HP-^{13}C imaging, showed $k_{PL\text{-}NAWM}$ = 0.017 s^{-1} ± 16.6% and $k_{PB\text{-}NAWM}$ = 0.0045 s^{-1} ± 25.1% (mean ± CV) over 2 scans spanning 224 days. Despite focal RT and surgery between the second and last timepoints, patient P1 also demonstrated similar values of $k_{PL\text{-}NAWM}$ = 0.017 s^{-1} ± 7.3% and $k_{PB\text{-}NAWM}$ = 0.0053 s^{-1} ± 34.0% (mean ± CV), which were consistent over 3 scans spanning 525 days.

3.3. Effects of radiation and chemotherapy (TMZ)

In the 3 patients who received RT and/or TMZ during serial imaging as part of treatment, values of $k_{PL\text{-}NAWM}$ were comparable across scans. With adjuvant RT, patients P1 and P5 showed pre/post-radiotherapy $k_{PL\text{-}NAWM}$ = 0.016 ± 0.001/0.016 ± 0.001 s^{-1} and 0.028 ± 0.001/0.025 ± 0.002 s^{-1} (± error), with the last scans being 39 and 33 days after RT, respectively. For two separate RT + TMZ treatments, patient P2 showed pre/post-chemoradiotherapy $k_{PL\text{-}NAWM}$ = 0.021 ± 0.001/0.020 ± 0.001 s^{-1} and 0.019 ± 0.001/0.022 ± 0.001 s^{-1} (± error), with the last scans being 78 and 15 days after therapy, respectively.

3.4. Effects of anti-angiogenic therapy

Patient P2 presented an interesting case study on the effects of treatment and the associated evolution of kinetic profiles within presumed tumor regions. In Fig. 4A, the $k_{PL\text{-}NAWM}$, $k_{PL\text{-}T2L}$ and $k_{PL\text{-}CEL}$ are shown together as colored traces for each of 9 scans that spanned 512 days, alongside a treatment axis detailing clinical management. Over the first 6 exams, the $k_{PL\text{-}NAWM}$ indicated by the blue trace was longitudinally consistent within 6.8% (CV), despite treatment with RT/TMZ. However, $k_{PL\text{-}T2L}$ and $k_{PL\text{-}CEL}$, shown as red and orange traces, respectively, displayed elevations above $k_{PL\text{-}NAWM}$ and dynamic changes during the same treatment interval. With the development of a new enhancing lesion at the fifth timepoint (TP5) that persisted through the next scan (TP6), there is a corresponding increase in $k_{PL\text{-}T2L}$ (8–11%) and $k_{PL\text{-}CEL}$ (82–92%) above $k_{PL\text{-}NAWM}$. Upon initiation of the anti-angiogenic agent bevacizumab, the enhancing lesion resolved at the seventh timepoint (TP7), while k_{PL} increased globally. The elevation in

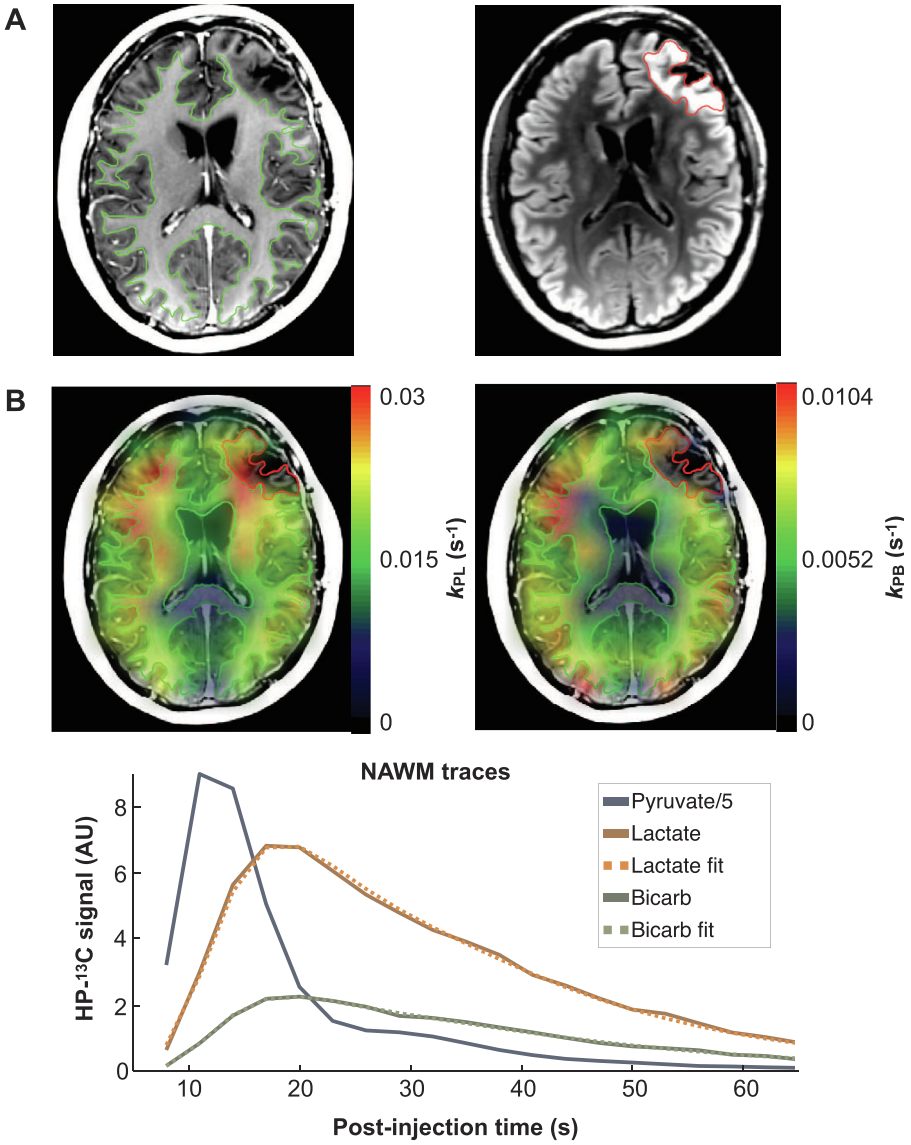

Fig. 2. Example HP-^{13}C kinetic maps. Regions of interest from a patient with GBM: NAWM (*green*) and T2L (*red*) overlaid on T_1-weighted IRSPGR and T_2-weighted FLAIR images, respectively (A). Maps of k_{PL} and k_{PB} based on kinetic modeling of dynamic HP-^{13}C EPI data overlaid on the same T_1-weighted images (B, *top*). Corresponding dynamic traces of HP [1-^{13}C]pyruvate, [1-^{13}C]lactate, and [^{13}C]bicarbonate signal within NAWM are shown alongside kinetic model fits (B, *bottom*). (For interpretation of the references to colour in this figure legend, the reader is referred to the web version of this article.)

$k_{PL\text{-}NAWM}$ reached a maximum of 0.047 ± 0.001 s^{-1} (± error) at 62 days (TP8) after the first bevacizumab infusion, a 134% increase over mean $k_{PL\text{-}NAWM}$ prior to treatment with bevacizumab. An analogous global increase in $k_{PB\text{-}NAWM}$ showed a maximum value of 0.011 ± 0.001 s^{-1} at the same time.

Fig. 4B shows the corresponding k_{PL} maps overlaid on T_1-weighted images for timepoints 5–8, which demonstrated elevated k_{PL} within the new enhancing lesion and the drastic global change in k_{PL} following bevacizumab treatment. Approximately the same maximum value of $k_{PL\text{-}NAWM}$ (0.047 ± 0.003 s^{-1}) was observed in patient P3 62 days after bevacizumab treatment, representing a 198–234% elevation above prior scans. Fig. 4C depicts the dynamic EPI traces for each metabolite in NAWM from Fig. 4A,B before and after bevacizumab. While the SNR was overall lower at the post-bevacizumab timepoint, signal from both [1-^{13}C]lactate and [^{13}C]bicarbonate was proportionally higher relative to [1-^{13}C]pyruvate.

3.5. Profiles of progression

Patients P2, P4, and P5 developed radiological progression over the course of serial imaging, which was characterized by elevation of $k_{PL\text{-}T2L}$, and $k_{PL\text{-}CEL}$ in particular, relative to $k_{PL\text{-}NAWM}$. Patient P2 exhibited a mean ratio of $k_{PL\text{-}CEL}/k_{PL\text{-}NAWM}$ = 1.77 from 3 to 6 cm^3 of multi-focal gadolinium-enhancing lesions, with individual lesion $k_{PL\text{-}CEL}$ ranging from 0.032 ± 0.008 s^{-1} to 0.041 ± 0.009 s^{-1} (± error) over 3 scans (Table 2). In the case of patient P5, the 12 cm^3 pre-surgical enhancement showed a ratio of $k_{PL\text{-}CEL}/k_{PL\text{-}NAWM}$ = 1.42 and $k_{PL\text{-}CEL}$ = 0.040 ± 0.003 s^{-1} (Table 2). The mean ratio of $k_{PL\text{-}T2L}/k_{PL\text{-}NAWM}$ was 1.16 and 0.95 for patients P2 and P5, respectively (Table 2). In contradistinction with other patients who progressed, patient P4 manifested an entirely non-enhancing lesion (87 cm^2) with $k_{PL\text{-}T2L}/k_{PL\text{-}NAWM}$ = 1.29 and $k_{PL\text{-}T2L}$ = 0.024 ± 0.001 s^{-1}. Progression timepoints for these patients are depicted in Fig. 5 with k_{PL} maps overlaid on T_2-weighted FLAIR and post-gadolinium T_1-weighted images. For patient P5, the k_{PL} within the lesion was elevated relative to NAWM, and also displayed spatial heterogeneity: the highest values were in and

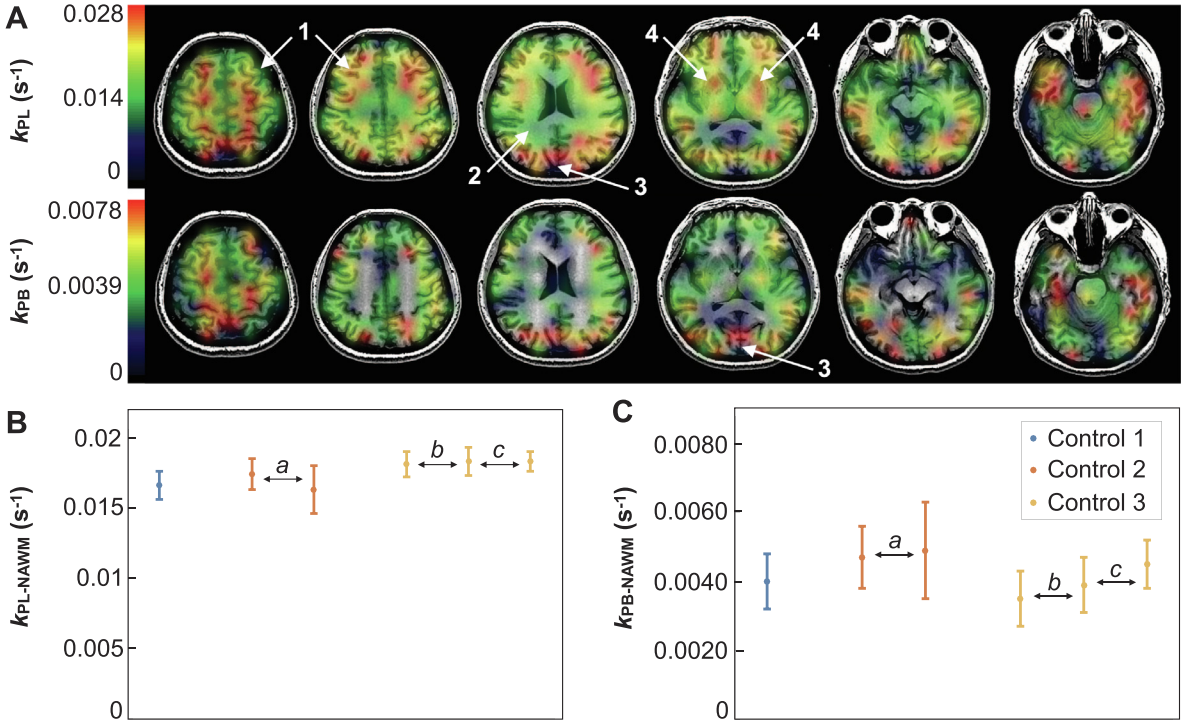

Fig. 3. Volunteer HP-^{13}C kinetic data. Maps of k_{PL} and k_{PB} from the third scan of healthy volunteer HV3 overlaid on T_1-weighted images, which illustrate the spatial variation of apparent HP [1-^{13}C]pyruvate metabolism: *1*, cortex/grey matter; *2*, white matter; *3*, cuneus; and *4*, putamen/deep grey matter (A). Healthy volunteer values of $k_{PL\text{-}NAWM}$ (B) and $k_{PB\text{-}NAWM}$ (C) are shown together with nonlinear least squares fitting error for 3 subjects over scan intervals of 30 min (*a*), 107 days (*b*) and 67 days (*c*).

around the CEL, while the surrounding T2L k_{PL} was comparatively lower (Fig. 5A). Patient P2 likewise demonstrated an anatomical lesion with elevated k_{PL} that, in this example, extended beyond the CEL margins into the non-enhancing T2L (Fig. 5B). The entirely non-enhancing T2L of patient P4 displayed corpus collosum involvement that extended to the left frontal cortex and white matter, along with diffusely elevated k_{PL} in the same region (Fig. 5C).

3.6. Quantifying lesion k_{PB}

While $k_{PL\text{-}T2L}$ and $k_{PL\text{-}CEL}$ were quantifiable, estimates of lesion k_{PB} demonstrated errors exceeding 25% in all but one scan due to the low ^{13}C bicarbonate signal within the T2L relative to NAWM. Supplementary Fig. 3 illustrates the characteristically reduced metabolite signal in a radiologically stable T2L compared to the contralateral hemisphere for summed metabolite data with SNR > 3. These data from patient P2 display less conversion of [1-^{13}C]pyruvate to [^{13}C]bicarbonate within the T2L, but are below the noise floor and thus cannot inform on the relative metabolic rate, k_{PB}.

3.7. Evaluating exam quality

Analysis of the experimental parameters for patient P2, who demonstrated low CVs for $k_{PL\text{-}NAWM}$ (6.8%) and $k_{PB\text{-}NAWM}$ (10.6%) over 6 scans, provided a framework to evaluate exam quality. QC parameters maintained for these 6 scan injections were: polarization > 33%, pyruvate concentration > 224 mM, and time-to-injection ≤55 s. Within NAWM, the median total voxel SNR ranged 9.7–24.4 ([1-^{13}C]lactate) and 5.5–7.9 ([^{13}C]bicarbonate) for 3.38–8 cm^3 spatial resolution, and allowed for rate constant errors of 2–6% ($k_{PL\text{-}NAWM}$) and 7–9% ($k_{PB\text{-}NAWM}$). Because [^{13}C]bicarbonate is the resolution-limiting metabolite, it was determined that achieving a median voxel SNR ≥5.5 for [^{13}C]bicarbonate enabled ideal quantification error ($k_{PB\text{-}NAWM}$ error < 7%) with the 1.5 cm isotropic resolution (3.38 cm^3).

Table 2
HP-^{13}C kinetic data. Rate constants modeled from serial HP-^{13}C data are shown for healthy volunteers (HV) and patients (P) within regions of interest.

SubjectID	$k_{PL\text{-}NAWM}$ (s^{-1}) median (range)	$k_{PL\text{-}T2L}$ (s^{-1}) median (range)	$k_{PL\text{-}CEL}$(s^{-1}) median (range)	$k_{PB\text{-}NAWM}$ (s^{-1}) median (range)	Mean $k_{PL\text{-}T2L}/k_{PL\text{-}NAWM}$	Mean $k_{PL\text{-}CEL}/k_{PL\text{-}NAWM}$	$k_{PL\text{-}NAWM}$, $k_{PB\text{-}NAWM}$ CV (%)
HV1-3	0.018 (0.016–0.018)	NA	NA	0.0043 (0.0035–0.0049)	NA	NA	5.0, 12.6
P1	0.016 (0.016–0.018)	0.013 (0.013–0.013)	NA	0.0047 (0.0039–0.0074)	0.76	NA	7.3, 34.0
P2	0.021 (0.019–0.047)	0.025 (0.018–0.036)	0.035 (0.032–0.041)	0.0076 (0.0062–0.011)	1.16	1.77	6.8*, 10.6*
P3	0.016 (0.014–0.047)	0.021 (0.012–0.51)	0.018 (0.012–0.051	0.0064 (0.0042–0.0069)	1.09	1.01	8.0*, 29.4*
P4	0.017 (0.015–0.019)	0.022 (0.020–0.024)	NA	0.0045 (0.0037–0.0053)	1.30	NA	16.6, 25.1
P5	0.029 (0.025–0.029)	0.027 (0.021–0.031)	0.04	0.0059 (0.0033–0.0079)	0.95	1.42	7.1, 40.7

*CVs for 6 (P2) and 2 (P3) scans without bevacizumab treatment.

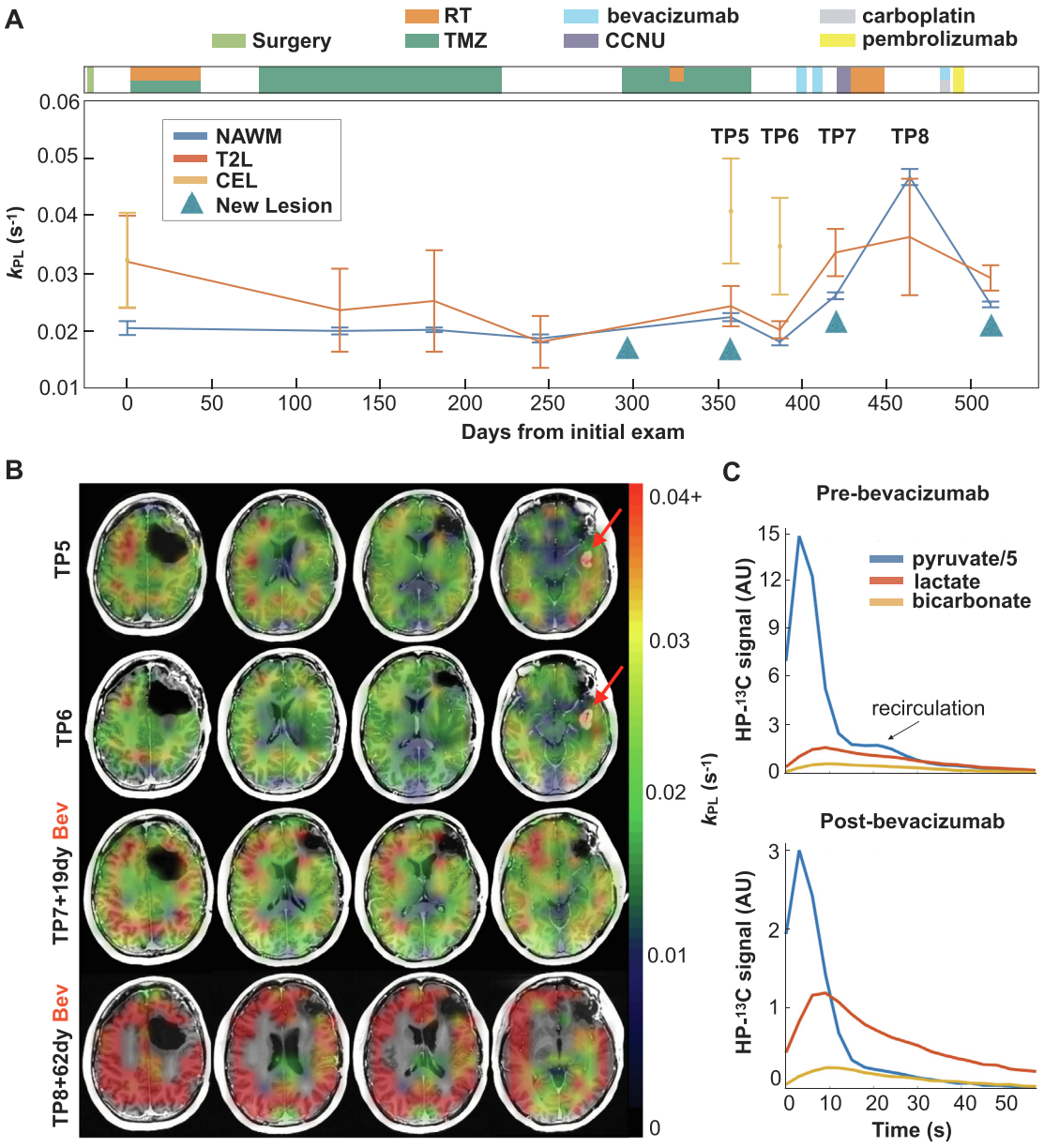

Fig. 4. Effects of bevacizumab. Serial k_{PL} data within NAWM and presumed tumor regions are shown for patient P2 over 9 scans spanning 512 days, along with clinical treatment information (A). Values of $k_{PL\text{-}NAWM}$ (*blue*) remained consistent until the administration of bevacizumab, whereupon a global increase in k_{PL} occurred, as seen at timepoint 8 (TP8) (A). Both $k_{PL\text{-}T2L}$ (*red*) and $k_{PL\text{-}CEL}$ (*orange*) are seen to be elevated relative to $k_{PL\text{-}NAWM}$, particularly at the time of progression. Corresponding k_{PL} maps for timepoints TP5-TP8 overlaid on T_1-weighted images illustrate the emergence of a new gadolinium-enhancing lesion with elevated k_{PL} (red arrows), which disappeared following treatment with bevacizumab, and subsequent global elevation of k_{PL} (B). Kinetic traces from pre- and post-bevacizumab scans demonstrate lower overall HP signal with bevacizumab, but proportionally greater [1-^{13}C]lactate and [^{13}C]bicarbonate signal relative to that of [1-^{13}C] pyruvate (C). (For interpretation of the references to colour in this figure legend, the reader is referred to the web version of this article.)

4. Discussion

This study characterized serial dynamic HP-^{13}C imaging of the brain in healthy volunteers and patients who underwent treatment for infiltrating glioma. Kinetic modeling of apparent [1-^{13}C]pyruvate metabolism within NAWM demonstrated relatively consistent values of rate constants across subjects over multiple exams and extended intervals. While patients displayed longitudinal consistency in $k_{PL\text{-}NAWM}$ irrespective of various treatments, the initiation of anti-angiogenic therapy coincided with the global elevation of rate constants. In cases of progressive disease, anatomic lesions showed elevated k_{PL} relative to that in the NAWM, which may reflect aberrant metabolism.

The consistency of NAWM kinetics in healthy volunteers is noteworthy, given the importance of establishing an appropriate reference for defining pathological changes in [1-^{13}C]pyruvate metabolism. These findings also agree with results from a prior study utilizing a model-based spectroscopic imaging approach: the mean $k_{PL\text{-}NAWM}$ and $k_{PB\text{-}NAWM}$ in 4 healthy subjects was 0.012 s^{-1} ± 6% and 0.002 s^{-1} ± 100% (± CV), respectively, compared to 0.018 s^{-1} ± 5.0% and 0.0043 s^{-1} ± 12.6% reported here (Grist et al., 2019). While kinetic parameter values can vary according to the echo time and signal weighting of the imaging sequence, the relative ranges of $k_{PL\text{-}NAWM}$ in both studies provided evidence of inter-subject consistency (Chen et al., 2019). Because [^{13}C]bicarbonate detection relies on the effective SNR that can be achieved within the experimental framework, a variety of factors may have influenced the variability in

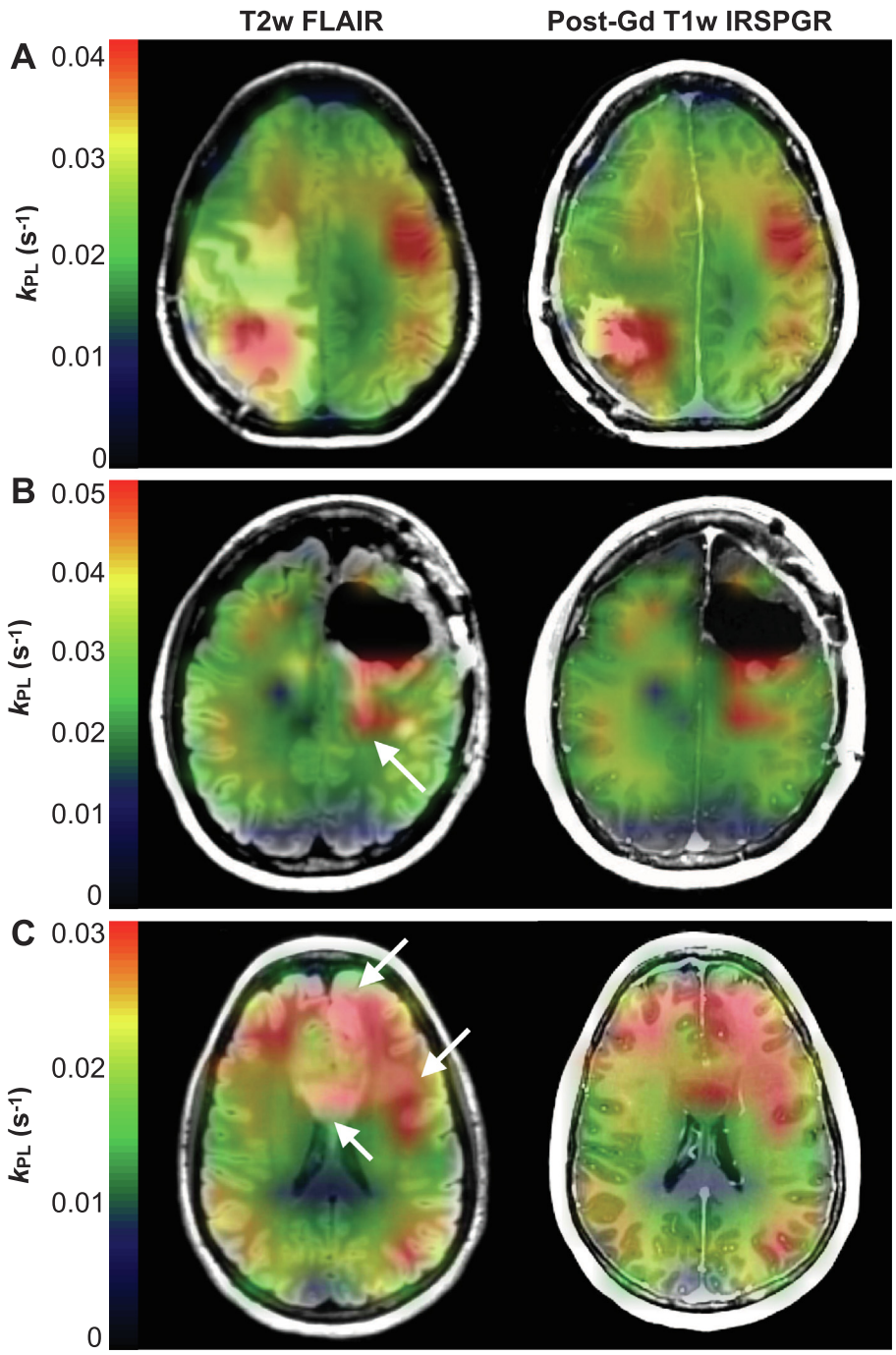

Fig. 5. Profiles of progression. Imaging at the time of radiologically-defined progression shown using k_{PL} maps overlaid on T_2-weighted FLAIR and post-gadolinium T_1-weighted images. Patient P5 demonstrated elevated k_{PL} in the lesion that was spatially heterogeneous, with higher values in and around the CEL compared to the surrounding T2L (A); whereas patient P2 showed uniformly elevated k_{PL} that extended distally from the CEL into the T2L, as indicated by the white arrow (B). Diffusely elevated k_{PL} in patient P4 corresponded with a large non-enhancing T2L centered in the corpus callosum and extending to the left frontal white matter and cortex (*white arrows*) (C). In each case, the lesion k_{PL} highlighted radiological progression.

quantification of $k_{PB\text{-}NAWM}$ from the prior study, including the use of a single channel volume coil versus a multi-channel phased array.

Based on the kinetic modeling of apparent metabolism over the course of serial HP-^{13}C imaging, patients also demonstrated consistent rate constants within NAWM. In the subject (P1) who received chemoradiotherapy prior to and RT during serial imaging, $k_{PL\text{-}NAWM}$ varied only slightly between scans, with the mean value being similar to that of healthy volunteers. Furthermore, interval changes in patient (P1, P2, P5) kinetics following limited RT or TMZ were not apparent within a routine 8 week window for clinical follow-up. These data, taken together with the overall consistency of $k_{PL\text{-}NAWM}$ observed in patients, suggest that NAWM may be a suitable reference region against which to compare alterations in [1-^{13}C]pyruvate metabolism. This is promising for potential applications geared toward monitoring response to therapy, since standard ^{1}H MRI cannot adequately distinguish treatment-induced changes from tumor (Winter et al., 2019; Da Cruz et al., 2011).

Although serial scans generally demonstrated longitudinal consistency, anti-angiogenic therapy appeared to produce global alterations in the rates constants. For two patients, the most pronounced increase in k_{PL} and k_{PB} followed an approximately 2-month interval from the initiation of bevacizumab. As a monoclonal antibody designed to normalize tumor vasculature through anti-VEGF activity, bevacizumab has become a tool for managing refractory brain edema and salvage therapy (Cuncannon et al., 2019). Because of its effective reduction of blood–brain barrier (BBB) permeability, gadolinium-enhancing lesions, which are the radiological hallmark of GBM, can often completely resolve, thus challenging clinical interpretations of tumor progression (Villanueva-Meyer et al., 2017). With regard to HP-^{13}C imaging, the data suggest that [1-^{13}C]pyruvate extravasation is reduced

as a result of vascular changes induced by bevacizumab, which cause conversion to downstream metabolites to appear more rapid by relative proportions. This is a plausible mechanism, given that [1-^{13}C]pyruvate is much smaller than the gadolinium chelates utilized by contrast agents, thereby allowing greater transport across the BBB under conditions of reduced permeability (Gerstner et al., 2019).

A critical finding in the three patients with progressive disease was that anatomic lesions manifested elevated k_{PL} compared to the surrounding NAWM. In each instance of gadolinium-enhancement, the CEL showed a regional k_{PL} maximum over the entire T2L, potentially indicating aberrant metabolism associated with disease, i.e., the Warburg effect and up-regulation of LDHA expression (Warburg, 1956; Valvona et al., 2016). Although there is evidence of gadolinium deposition after contrast-enhanced MRI (McDonald et al., 2015), signal loss due to potential deposition over serial exams is not a concern for HP imaging because the relaxivity of commercial gadolinium-based contrast agents is substantially lower on ^{13}C than water (Gabellieri and Leach, 2009; Smith et al., 2012). The heterogeneity of k_{PL} observed across the anatomic lesion in patient P5 may be reflective of the underlying features of GBM metabolism and the spatial extent of disease within the T2L, which cannot be distinguished from vasogenic edema on routine imaging. Such edema reduces normal perfusion (Bastin et al., 2006) in a manner that appeared to lower [1-^{13}C]pyruvate signal and apparent conversion in this study, and thus requires careful evaluation. Patient P2 additionally demonstrated a non-enhancing T_2-hyperintense lesion with elevated $k_{PL\text{-}T2L}$ during the initial progression, which may have indicated infiltrative disease. Even the entirely non-enhancing lesion of patient P4 displayed diffuse elevation of $k_{PL\text{-}T2L}$ that provided evidence of metabolic abnormality in low-grade disease. These results were obtained in the challenging post-treatment context, where lesions typically present with less volume and gadolinium-enhancement than newly diagnosed disease. Nonetheless, the findings support the potential utility of HP-^{13}C imaging in differentiating treatment-induced changes from progressive enhancing or non-enhancing tumor.

While k_{PB} was readily quantified in NAWM, estimates of lesion values were challenging owing to the lower [^{13}C]bicarbonate signal. This comparatively lower signal in the T2L at a voxel-wise level provided evidence of less conversion from [1-^{13}C]pyruvate and reduced TCA cycle metabolism (Martinez-Reyes and Chandel, 2020), which is itself an important observation concerning the influence of edema and tissue environment. Whether certain gliomas display measurably reduced k_{PB} as part of a malignant metabolic phenotype remains to be determined.

Using the data from patient P2,who demonstrated low CVs over serial scans, it was possible to provide experimental guidelines for achieving adequate SNR. From a QC standpoint, maintaining a time-to-injection $\leq$55 s preserved enough hyperpolarization to obtain reliable data at higher resolutions. Furthermore, the isotropic spatial resolution of 1.5 cm (3.38 cm^3) demonstrated sufficient SNR (median voxel SNR $\geq$5.5 in NAWM) for quantification, based on the model fitting error for [^{13}C]bicarbonate, which limits resolution. This resolution also represented a practical tradeoff with model error to maintain repeatability, and not necessarily an absolute limit.

In this study, a first-order, single compartment model was able to consistently quantify k_{PL} and k_{PB} in high-quality datasets, however it is worth noting the potential influence of certain biological factors. The measured signals are a combination of vascular and intracellular/extracellular metabolite pools and depend on compartmentalized ^{13}C-label exchange (Bankson et al., 2015). Thus, highly perfused tumor can appear to have lower rate constants by comparison to regions that display normal perfusion when vascular [1-^{13}C]pyruvate is not excluded. Additionally, there are a number of the factors influencing ^{13}C-label exchange via enzymatic conversion: while k_{PL} has been shown to correlate with LDH, pre-clinical studies have shown that values of k_{PL} can also be influenced by the pyruvate delivery rate, vascular/cellular compartment permeability, monocarboxylate transporter (MCT) expression/activity, metabolite pool sizes, LDH expression/activity, associated cofactor nicotinomide adenine dinucleotide (NADH) levels, and cellularity (Bankson et al., 2015; Hurd et al., 2010). Although overexpression of MCT4 in GBM (Miranda-Goncalves et al., 2013) may facilitate lactate efflux, the “pool size effect” of excess endogenous lactate from LDH overexpression/hyperactivity likely promotes elevated k_{PL} relative to healthy tissue (Day et al., 2007). Since this study did not account for nonlinear enzyme reaction velocities described by Michaelis-Menten kinetics under conditions of sufficiently high substrate concentration, deviations related to pyruvate saturation effects were possible (Xu et al., 2011).

Further interrogating [1-^{13}C]pyruvate metabolism in patients with glioma will entail a variety of tactics that are aimed at improving both analysis and methodology. From an analysis standpoint, the application of the inputless kinetic model provided regionally consistent measures of apparent rate constants. While proving largely robust to variations in receiver hardware, it may have been affected by changes in the acquired spatial resolution and flip angle scheme over the developmental phase of the study, owing to partial volume effects in the first case and model limitations in the second. Most of the intra-subject variability likely resulted from lower SNR in the data with higher than 1.5 cm isotropic resolution or changing flip angle schemes between serial scans. With a variable resolution (Gordon et al., 2018) acquisition scheme, resolution could be defined independently for each metabolite on the basis of SNR, thereby improving [^{13}C]bicarbonate measurement and k_{PB} quantification. Being able to extend quantification with an accounting of the vascular contributions of [1-^{13}C]pyruvate, and to a lesser extent [1-^{13}C]lactate (Chaichana et al., 2010), will enhance the ability to detect aberrant metabolism and potentially monitor response to treatment. Because of the strong dependence on SNR for quantifying HP data and resolving finer regions of metabolism, additional hardware and reconstruction improvements will be critical to clinically translating this technology (Crane et al., 2020). Implementing atlas-based prescription routines for HP acquisitions would also augment the ability to compare data longitudinally on a voxel-wise basis (Bian et al., 2018). Furthermore, by enrolling larger cohorts of patients with newly diagnosed disease and age-matched controls the range of population differences can be characterized along with metabolism associated with disease.

5. Conclusion

Kinetic modeling of serial HP-^{13}C data from patients with glioma demonstrated consistent values of rate constants $k_{PL\text{-}NAWM}$ and $k_{PB\text{-}NAWM}$ longitudinally, which were mostly similar to those of healthy volunteers. The anti-angiogenic agent bevacizumab appeared to be associated with a global elevation of apparent rate constants that may have resulted from reduced extravasation of [1-^{13}C]pyruvate through the BBB. In patients with progressive disease, the k_{PL} was also elevated in both gadolinium-enhancing and non-enhancing lesions, potentially highlighting aberrant metabolism across a range of glioma subtypes and supporting the utility of HP-^{13}C imaging.

CRediT authorship contribution statement

Adam W. Autry: Conceptualization, Methodology, Formal analysis, Writing - original draft. **Jeremy W. Gordon:** Conceptualization, Methodology, Writing - review & editing. **Hsin-Yu Chen:** Methodology, Writing - review & editing. **Marisa LaFontaine:** Writing - review & editing. **Robert Bok:** Writing - review & editing. **Mark Van Criekinge:** Resources, Writing - review & editing. **James B. Slater:** Resources, Writing - review & editing. **Lucas Carvajal:** Resources, Writing - review & editing. **Javier E. Villanueva-Meyer:** Conceptualization, Writing - review & editing. **Susan M. Chang:** Conceptualization, Funding acquisition, Writing - review & editing. **Jennifer L. Clarke:** Conceptualization, Funding acquisition, Writing - review & editing.

Janine M. Lupo: Conceptualization, Funding acquisition, Writing - review & editing. **Duan Xu:** Conceptualization, Writing - review & editing. **Peder E.Z. Larson:** Conceptualization, Methodology, Writing - review & editing. **Daniel B. Vigneron:** Conceptualization, Methodology, Funding acquisition, Writing - review & editing. **Yan Li:** Conceptualization, Supervision, Funding acquisition, Writing - review & editing.

Acknowledgements

This work is dedicated to the late professor Sarah J Nelson, and was supported by NIH Grants R01 CA127612, P01 CA118816, P41 EB0341598, P50 CA097257, and T32 CA151022, together with the Glioblastoma Precision Medicine Program.

Appendix A. Supplementary data

Supplementary data to this article can be found online at https://doi.org/10.1016/j.nicl.2020.102323.

References

Ardenkjaer-Larsen, J.H., Fridlund, B., Gram, A., et al., 2003. Increase in signal-to-noise ratio of > 10,000 times in liquid-state NMR. PNAS 100, 10158–10163.

Autry, A.W., Gordon, J.W., Carvajal, L., Mareyam, H., Chen, H.Y., Park, I., Mammoli, D., Vareth, M., Chang, S.M., Wald, L.L., Xu, D., Vigneron, D.B., Nelson, S.J., Li, Y., 2019. Comparison between 8- and 32-channel phased-array receive coils for in vivo hyperpolarized ^{13} C imaging of the human brain. Magn. Reson. Med. 82, 833–841.

Bankson, J.A., Walker, C.M., Ramirez, M.S., et al., 2015. Kinetic modeling and constrained reconstruction of hyperpolarized [1-13C]-pyruvate offers improved metabolic imaging of tumors. Cancer Res. 75 (22), 4708–4717.

Bastin, M.E., Carpenter, T.K., Armitage, P.A., Sinha, S., Wardlaw, J.M., Whittle, I.R., 2006. Effects of dexamethasone on cerebral perfusion and water diffusion in patients with high-grade glioma. AJNR 27 (2), 402–408.

Bian, W., Li, Y., Crane, J.C., Nelson, S.J.N., 2018. A fully automated atlas based method for prescribing 3D PRESS MR spectroscopic imaging: towards robust and reproducible metabolite measurements in human brain. Magn. Reson. Med. 79 (2), 636–642.

Chaichana, K.L., McGirt, M.J., Laterra, J., Olivi, A., Quinnones-Hinojosa, A., 2010. Recurrence and malignant degeneration after resection of adult hemispheric low-grade gliomas. J. Neurosurg. 112 (1), 10–17.

Chen, H.Y., Gordon, J.W., Bok, R., Cao, P., et al., 2019. Pulse sequence considerations for quantification of pyruvate-to-lactate conversion k_{PL} in hyperpolarized ^{13}C imaging. NMR Biomed. 32 (2), e4052.

Crane, J.C., Gordon, J.W., Chen, H,Y., Autry, A.W., et al., 2020. Hyperpolarized 13C MRI data acquisition and analysis in prostate and brain at University of California, San Francisco. NMR Biomed. 2020; e4280.

Cuncannon, M., Wong, M., Jayamanne, D., Guo, L., Cove, N., Wheeler, H., Back, M., 2019. Role of delayed salvage bevacizumab at symptomatic progression of chemorefractory glioblastoma. BMC Cancer 445.

Da Cruz, L.C.H., Rodriguez, I., Domingues, R.C., Gasparetto, E.L., Sorensen, A.G., 2011. Pseudoprogression and pseudoresponse: imaging challenges in the assessment of posttreatment glioma. AJNR 32 (11), 1978–1985.

Day, S.E., Kettunen, M.I., Gallagher, F.A., et al., 2007. Detecting tumor response to treatment using hyperpolarized 13C magnetic resonance imaging and spectroscopy. Nat. Med. 13, 1382–1387.

Gabellieri, C., Leach, M.O., Eykyn, 2009. Modulating the relaxivity of hyperpolarized substrates with gadolinium contrast agents. Contrast Media Mol. Imaging 4, 143–147.

Gerstner, E., Emblem, K.E., Chang, K., et al., 2019. Bevacizumab reduces permeability and concurrent temozolomide delivery in a subset of patients with recurrent glioblastoma. Clin. Cancer Res. 26, 206–212.

Golman, K., Zandt, R.I., Lerche, M., Pehrson, R., Ardenkjaer-Larsen, J.H., 2006. Metabolic imaging by hyperpolarized ^{13}C magnetic resonance imaging for in vivo tumor diagnosis. Cancer Res. 66, 10855–10860.

Gordon, J.W., Chen, H.Y., Autry, A., Park, I., Van Criekinge, M., Mammoli, D., et al., 2019. Translation of carbon-13 EPI for hyperpolarized MR molecular imaging of prostate and brain cancer patients. Magn. Reson. Med. 81, 2702–2709.

Gordon, J.W, Milshteyn, E., Vigneron Daniel, B., Larson Peder, E.Z., 2018. Variable Resolution Echo-Planar Imaging for Improved Quantification of Hyperpolarized 13C Metabolism. In Proceedings of the 26th Annual Meeting of ISMRM, Paris, France, 2018 (Abstract#3053).

Gordon, J.W., Vigneron, D.B., Larson, P., 2017. Development of a symmetric echo planar imaging framework for clinical translation of rapid dynamic hyperpolarized 13C imaging. Magn. Reson. Med. 77, 826–832.

Grist, J.T., McLean, M.A., Fiemer, F., Schulte, R.F., Deen, S.S., Zaccagna, F., et al., 2019. Quantifying normal human brain metabolism using hyperpolarized [1-13C]pyruvate and magnetic resonance imaging. NeuroImage 189, 171–179.

Hurd, R.E., Yen, Y.F., Tropp, J., et al., 2010. Cerebral dynamics and metabolism of hyperpolarized [1-(13)C]pyruvate using time-resolved MR spectroscopic imaging. J. Cereb. Blood Flow Metab. 30 (10), 1734–1741.

Jenkinson, M., Smith, S.M., 2001. A global optimisation method for robust affine registration of brain images. Med. Image Anal. 5, 143–156.

Larson, P.E.Z., Chen, H.Y., Gordon, J.W., Korn, N., Maidens, J., Arcak, M., Tang, S., Criekinge, M., Carvajal, L., Mammoli, D., Bok, R., Aggarwal, R., Ferrone, M., Slater, J.B., Nelson, S.J., Kurhanewicz, J., Vigneron, D.B., 2018. Investigation of analysis methods for hyperpolarized ^{13}C-pyruvate metabolic MRI in prostate cancer patients. NMR Biomed. 31 (11), e3997.

Lee, C.Y., Soliman, H., Geraghty, B.J., Chen, A.P., Connelly, K.A., Endre, R., Perks, W.J., Heyn, C., Black, S.E., Cunningham, C.H., 2020. Lactate topography of the human brain using hyperpolarized ^{13}C-MRI. NeuroImage 204, 116202.

Louis, D.N., Perry, A., Reifenberger, G., von Deimling, A., Figarella-Branger, D., Cavenee, W.K., Ohgaki, H., Wiestler, O.D., Kleihues, P., Ellison, D.W., 2016. The 2016 World Health Organization classification of tumors of the central nervous system: a summary. Acta Neuropathol. 31 (6), 803–820. https://doi.org/10.1007/s00401-016-1545-1.

Lunt, Y.L., Vander Heiden, M.G., 2011. Aerobic glycolysis: meeting the metabolic requirements of cell proliferation. Annu. Rev. Cell Dev. Biol. 27, 441–464.

Martinez-Reyes, I., Chandel, N.S., 2020. Mitochondrial TCA cycle metabolites control physiology and disease. Nat. Commun. 11 (102).

McDonald, R.J., McDonald, J.S., Kallmess, D.F., et al., 2015. Intracranial gadolinium deposition after contrast-enhanced MR imaging. Radiology 275 (3), 772–782.

Menze, B.H., Jakab, A., Bauer, S., Kalpathy-Cramer, J., Farahani, K., Kirby, J., et al., 2015. The multimodal brain tumor image segmentation benchmark (BRATS). IEEE Trans. Med. Imaging 34 (10), 1993–2024.

Miloushev, V.Z., Granlund, K.L., Boltyanskiy, R., et al., 2018. Metabolic imaging of the human brain with hyperpolarized ^{13}C pyruvate demonstrates ^{13}C lactate production in brain tumor patients. Cancer Res. 78, 3755–3760.

Miranda-Goncalves, V., Honavar, M., Pinheiro, C., et al., 2013. Monocarboxylate transporters (MCTs) in gliomas: expression and exploitation as therapeutic targets. Neuro Oncol. 15 (2), 172–188.

Park, I., Larson, P.E.Z., Tropp, L.T., et al., 2014. Dynamic hyperpolarized carbon-13 MR metabolic imaging of nonhuman primate brain. Magn. Reson. Med. 71 (1), 19–25.

Park, I., Larson, P.E.Z., Gordon, J.W., et al., 2018. Development of methods and feasibility of using hyperpolarized carbon-13 imaging data for evaluating brain metabolism in patient studies. Magn. Reson. Med. 80, 864–873.

Pruessmann, K.P., Wieger, M., Boernert, P., Boesiger, P., 2001. Advances in sensitivity encoding with arbitrary k-space trajectories. Magn. Reson. Med. 46, 638–651.

Saraste, M., 1999. Oxidative phosphorylation at the fin de siècle. Science 283 (5407), 1488–1493.

Smith, M.R., Peterson, E.T., Gordon, J.W., et al., 2012. In vivo imaging and spectroscopy of dynamic metabolism using simultaneous ^{13}C and ^{1}H MRI. IEEE Trans. Biomed. Eng. 59 (1), 45–49.

Stupp, R., Mason, W.P., van den Bent, M.J., Weller, M., Fisher, B., Taphoorn, M.J., et al., 2005. Radiotherapy plus concomitant and adjuvant temozolomide for glioblastoma. N. Engl. J. Med. 352 (10), 987–996.

Valvona, C.J., Fillmore, H.L., Nunn, P.B., Pilkington, G.J., 2016. The regulation and function of lactate dehydrogenase A: therapeutic potential in brain tumor. Brain Pathol. 26 (1), 3–17.

Villanueva-Meyer, J.E., Mabray, M.C., Cha, S., et al., 2017. Current clinical brain tumor imaging. Neurosurgery 81 (3), 397–415.

Wang, J., Wright, A.J., Hesketh, R.L., Hu, D., Brindle, K.M., 2017. A referenceless Nyquist ghost correction workflow for echo planar imaging of hyperpolarized [1-^{13}C]pyruvate and [1-^{13}C]lactate. NMR Biomed. 31 (2), e3866.

Warburg, O., 1956. On respiratory impairment in cancer cells. Science 124 (3215), 269–270.

Winter, S.F., Loebel, F., Loeffler, J., Batchelor, T.T., Martinez-Lage, M., Vajkoczy, P., Dietrich, J., 2019. Treatment-induced brain tissue necrosis: a clinical challenge in neuro-oncology. Neuro Oncol. noz048.

Xu, T., Mayer, D., Gu, M., et al., 2011. Quantification of in vivo metabolite kinetics of hyperpolarized pyruvate in rat kidneys using dynamic 13C MRSI. NMR Biomed. 24 (8), 997–1005.

Yan, H., Parsons, D.W., Jin, G., McLendon, R., Rasheed, B.A., Yuan, W., Kos, I., Batinic-Haberle, I., Jones, S., Riggins, G.J., Friedman, H., Friedman, A., Reardon, D., Herndon, J., Kinzler, K.W., Velculescu, V.E., Vogelstein, B., Bigner, D.D., 2019. *IDH1* and *IDH2* mutations in gliomas. N. Engl. J. Med. 360, 765–773.

Zhang, Y., Brady, M., Smith, S., 2001. Segmentation of brain MR images through a hidden random field model and the expectation maximization algorithm. IEEE Trans. Med. Imaging 20, 45–57.

Zihan, Z., Zhu, X., Ohliger, M.A., Tang, S., Cao, P., Carvajal, L., et al., 2019. Coil combination methods for multi-channel hyperpolarized ^{13}C imaging data from human studies. J. Magn. Reson. 301, 73–79.